

A hybrid tracking system for image-guided spine surgery using a tracked mobile C-arm: a phantom study

Peyman GHOBADI AZBARI^{1,2}, Alireza AHMADIAN^{1,2,*}, Hooshang SABERI^{3,4},
Mohammadreza AY^{1,5}, Mostafa ABDOLGHAFFAR^{1,2}, Keyvan AMINI KHOIY⁶

¹Department of Medical Physics and Biomedical Engineering, Faculty of Medicine, Tehran University of Medical Sciences, Tehran, Iran

²Research Center of Biomedical Technology and Robotics, Tehran University of Medical Sciences, Tehran, Iran

³Department of Neurosurgery, Imam Khomeini Complex Hospital, Tehran University of Medical Sciences, Tehran, Iran

⁴Brain and Spinal Injuries Repair Research Center, Imam Khomeini Complex Hospital, Tehran University of Medical Sciences, Tehran, Iran

⁵Research Center for Cellular and Molecular Imaging, Tehran University of Medical Sciences, Tehran, Iran

⁶Department of Biomedical Engineering, University of Akron, Akron, Ohio, USA

Received: 11.10.2014

Accepted/Published Online: 29.12.2015

Final Version: 24.01.2017

Abstract: In recent years, an increasing number of various surgeries are observed utilizing fluoroscopy. The radiation exposure received by patients and medical staff and the surgical guidance in multiple planes frequently necessitate the positioning of a mobile C-arm. Operative navigation enables a mobile C-arm to provide multiplanar surgical guidance and decreases the radiation dose to the patient and operating room personnel. In this study, we propose a video-based tracked mobile C-arm (referred to as a “tracked C-arm system”) to position the system. This system defines a reference framework to maintain the video-optical tracker data and computed tomography (CT) or cone-beam CT images’ alignment as fine as possible despite patient or tracker movement. By employing our uniquely designed “six-facet” reference marker attached to the spine phantom, registration between the video-optical tracker and the spine phantom is maintained at arbitrary angles of the mobile C-arm. The tracked C-arm system provides a statistically significant improvement ($P < 0.001$) in target registration error in comparison with the conventional system: 0.80 ± 0.34 mm versus 1.60 ± 0.43 mm, respectively. The tracked C-arm system is designed to generate digitally reconstructed radiograph images from the mobile C-arm perspective, with projection error on the order of 0.74 ± 0.13 mm. Integration of the hybrid tracking system with mobile C-arm guidance has the capability to provide registration, reduce radiation exposure, and improve target registration accuracy.

Key words: Tracked C-arm system, video-optical tracker, Pseudo C-arm Simulator, image guided surgery, artificial fluoroscopy

1. Introduction

Image-guided surgery approaches generally use a combination of preoperative image data in combination with intraoperative tool tracking. While such methods have facilitated tremendous advances in surgical techniques, the recent intraoperative imaging provides up-to-date 3D intraoperative images during the navigation process. A mobile C-arm is an intraoperative imaging system that is based on X-ray technology and can be used in

*Correspondence: ahmadian@tums.ac.ir

various fields such as surgery, orthopedics, traumatology, vascular surgery, and cardiology. With the growing development of minimally invasive surgeries, the use of computed tomography (CT) and fluoroscopic guidance is evolving in a wide variety of procedures [1–4].

Previous studies have proposed navigation incorporating a C-arm imaging and tracking system [5–10]. In such systems, the tracker is located at a distance of 100–200 cm from the operating table. Although these systems provide more accurate access trajectories (e.g., [11–13] for pedicle screws in spinal surgery), they have some drawbacks, including line-of-sight occlusion due to personnel presence around the surgical operating table, invasive registration, and the use of a dynamic reference base. The latter two points are the main drawbacks of these systems. Combined use of the tracking system and mobile C-arm with cone-beam CT (CBCT) reconstruction capability provides navigation and visualization using up-to-date 3D images [6–10]. The system is referred to as registration-free navigation [6,14]. Feuerstein et al. [10] superimposed laparoscopic data with CBCT data within a registration-free navigation frame. This method combines intraoperative CBCT imaging, tracking, and visualization to display the organ's motion between intraoperative and preoperative imaging virtually.

Positioning fluoroscopic devices in the desired place can be a time-consuming task and they require multifold fluoroscopic acquisitions. Therefore, artificial fluoroscopy is used for fluoroscopy time reduction and target localization. Artificial fluoroscopy enables a mobile C-arm to provide real-time and multiple-plane procedural guidance by combining the mobile C-arm with a tracking system. It also decreases the radiation exposure of patients and medical staff by eliminating the need to reposition the fluoroscope repeatedly to obtain surgical guidance in tool placement [5]. Dressel et al. [15] proposed an extended combination of mobile C-arm and artificial fluoroscopy to provide position data. The approach is based on the estimate of the mobile C-arm motion and is achieved using a camera-augmented mobile C-arm system [16] wherein a video camera and a double mirror construction were placed on the C-arm X-ray tube to fuse X-ray and optical images.

The system described in this study presents a new combination of the video-optical tracker and the mobile C-arm. Unlike a conventional system in which the video optical tracker is located outside the surgical field, the proposed configuration places the video-optical tracker on the C-arm system at a distance of 60 cm from the rotation center of the C-arm, which improves the geometric accuracy and reduces the line-of-sight obstruction. The challenge of retaining registration within a circular framework is resolved by a “six-facet” reference marker. In addition, the proposed combination enables digitally reconstructed radiograph (DRR) generation of the 3D image data to visualize the projection perspectives without X-ray exposure. The proposed system performance has been assessed based on the target registration error (TRE) and projection error.

2. Materials

2.1. Pseudo C-arm Simulator (PCS)

In the first stage of this work, a Pseudo C-arm Simulator (PCS) was designed to simulate circular movement of the C-arm system. Figure 1 shows the PCS setup. The video-optical tracker is then placed directly on the PCS setup at a distance of approximately 60 cm from the rotation center of the simulator. By attaching a “six-facet” reference marker to the spine phantom, the registration between the tracker and spine phantom is maintained at PCS setup arbitrary angles. The PCS setup is made up of a video-optical tracker, motorized rotation, and trolley. Hence, the proposed combination creates tracking capability at any PCS setup rotation angle.

2.2. “Six-facet” reference marker

The reference marker defines the coordinate system associated with the patient. Hence, it provides a reference framework to maintain registration notwithstanding movement of the spine phantom or video-optical tracker. The pointer size and the need to have knowledge about the line-of-sight are the main challenges for the designed markers to be visible from various angles of the PCS or tracked C-arm setups. A “six-facet” reference marker comprises a hexahedron attached to six Plexiglas sheets aligned in a hexagon shape. Each face has a specific pattern, which is detected by the video-optical tracker.



Figure 1. Illustration of the proposed hybrid system. The video-optical tracker is attached directly on the Pseudo C-arm Simulator.

Each facet contains a specific spatial arrangement of Xpoints defining the coordinate system associated with each facet, as shown in Figure 2a. The size and arrangement of the Xpoints are found by reiterative experiments.

Registration between the video-optical tracker and the patient is retained at any angle of the PCS or Tracked C-arm setups using a “six-facet” reference marker firmly fixed to the spine phantom.

2.3. Tracking system

The Micron Tracker video-optical tracker under Parsiss IV Optic Vision is used in this research, as shown in Figure 2b, which provides a video stream of the surgical field. The video-optical tracker makes a FOM of about 30–290 cm in distance from the video-optical tracker at a rate of 16 Hz, and a video stream of 1280×960 pixels.

2.4. Mobile C-arm

The C-arm used in the experiments is an ARCADIS Orbic 3D from Siemens Medical Solutions USA, Inc. The system used in our proving ground for spine phantom study is shown in Figure 2c. The ARCADIS Orbic produces 3D images straight in the surgery room. In addition, the ARCADIS Orbic 3D has an isocentric plane and 190° ($+95^\circ / -95^\circ$) orbital motion. The 3D capability of ARCADIS Orbic 3D is appropriate in a wide range of intraoperative orthopedic applications and trauma surgical operations of the spine.

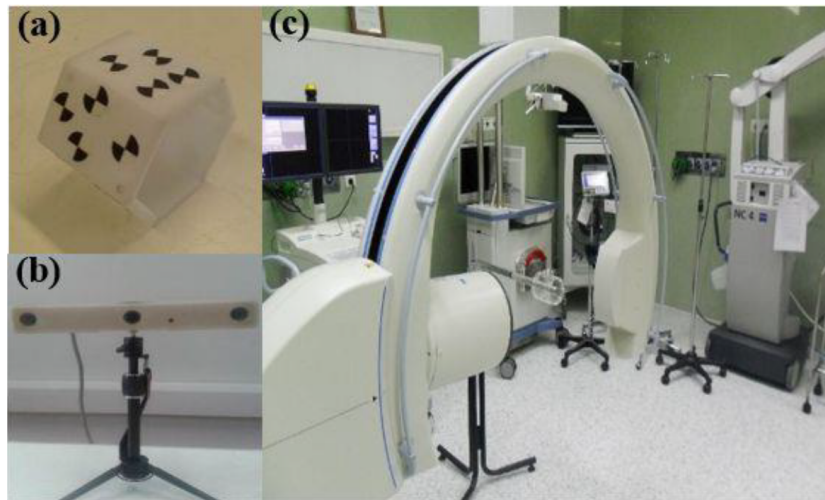


Figure 2. a) Schematic of the “six-facet” reference marker, b) video-optical tracker (Micron Tracker H3-60, Claron Inc., Toronto, ON, Canada), c) C-arm system (ARCADIS Orbic 3D, Medical Solutions USA, Inc.).

2.5. Spine phantom

Our experiments were carried out on a spine phantom containing 12 surface markers. Six markers in the spine phantom are selected as targets, and the other six markers are used as fiducial markers in order to point-based register the video-optical tracker data with CT images. Figure 3 shows that surface landmark points of the spine phantom were acquired using a tracking tool equipped with tracker-distinguishable patterns. The video optical tracker detects the checker board patterns that are fixed on the tool to determine the position of the target touched by the tool tip. To obtain the surface points, a “six-facet” reference marker is firmly fixed to the spine phantom by holder base, as shown in Figure 3. The coordinates of points were recorded towards both the camera and the reference.



Figure 3. A “six-facet” reference marker is fixed on the spine phantom along with an example tracking tool.

2.6. Calibration-phantom

An improved edition of the calibration-phantom [17] was created proportionate to the C-arm FOV. The calibration-phantom consists of 20 stainless steel spheres, which are divided into two groups: a group of 16 stainless steel spheres are placed in two orbital patterns placed in a Plexiglas cylinder, and a group of 4 stainless steel spheres are placed at the Xpoint centers in a firmly attached reference marker, as shown in Figure 4a. Each orbital pattern includes eight stainless steel spheres, which are uniformly distributed over 360° . The diameter of each stainless steel sphere is 4.713 mm, the diameter of each orbital pattern is 100 mm, and the distance between the two parallel orbital patterns is 160 mm (changes in the sizes of orbital patterns and stainless steel spheres are supported by appropriate settings of algorithm constant coefficients). A CBCT reconstruction of the calibration-phantom was obtained to specify the stainless steel sphere positions in the coordinate system of the CBCT data as illustrated in Figure 4b.

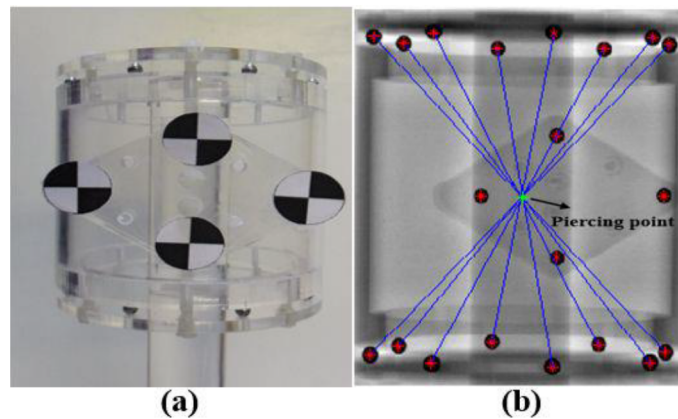


Figure 4. a) Calibration-phantom, b) radiographic image of the calibration phantom.

3. Methods

Figure 5 displays the schematic of the hybrid system. The general procedure of the hybrid system includes the following steps: CT image acquisition of the spine phantom, fixation of the “six-facet” reference marker to the spine phantom, geometric calibration of the mobile C-arm, registration, pose estimation, and artificial fluoroscopy.

The methodology used for the hybrid system includes the following steps: registration procedure, geometric calibration, and the generation of DRRs from the C-arm perspective.

3.1. Registration

First, surgical instrument tracking determines the location and orientation of the patient and surgical instruments in the world coordinate system. Then a registration process is used to establish the relation between the 3D volume images and the world coordinate system, and eventually it shows the navigated surgical instrument position in the 3D volume images. We employed a paired-point registration approach [18] to estimate the translation vector and rotation matrix. This method iteratively finds corresponding points with respect to the minimum distance between them. These points are mapped to each other using a least squares algorithm. The fiducial registration error (FRE), which is the distance between the corresponding fiducial markers [19], was calculated and reported with the Parsiss Image-Vision navigation system (Parseh Intelligent Surgical System

Company, Parsiss Co., Tehran, Iran). This error is sometimes reported for systems that obtain registration by aligning pairs of fiducial points in both spaces.

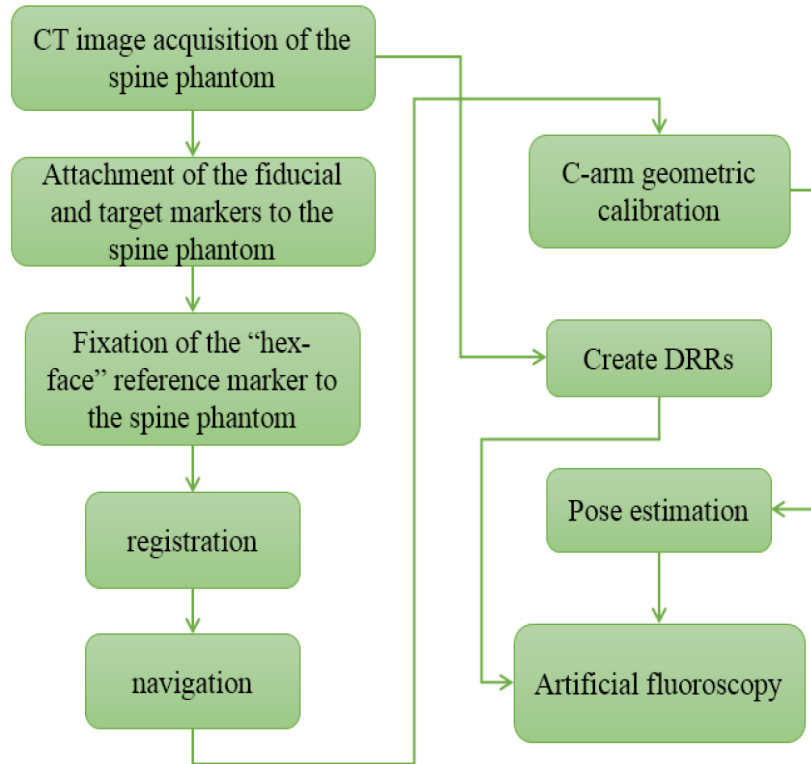


Figure 5. Block diagram of workflow of the hybrid system.

Geometric accuracy is assessed based on TRE, using the root mean square formula (RMS) specified as the distance between the physical target (pt) points and the corresponding target marker (tm) points defined on a medical image after registration:

$$TRE = [(X_{tm} - X_{pt})^2 + (Y_{tm} - Y_{pt})^2 + (Z_{tm} - Z_{pt})^2]^{1/2} \quad (1)$$

where X, Y, and Z indicate the coordinates of the point. For each anatomical landmark distribution, the best submillimeter accuracy of FRE was obtained and the TRE values were calculated thereafter. Figure 6 shows both the FRE and TRE.

Using the FRE values reported by the navigation system, the prediction TRE(r) at point r can be computed by the following formula [20]:

$$TRE^2(r) \approx \frac{FRE^2}{N-2} \left(1 + \frac{1}{3} \sum_{k=1}^3 \frac{d_k^2}{f_k^2} \right) \quad (2)$$

where N is the number of fiducials, d_k are the target distances from the main axis 'k', and f_k is the distance from fiducials to the main axis 'k'.

The predicted TRE depends on various factors such as the number of fiducials (N) and the configuration of the fiducials. According to this formula, increasing the distance between each fiducial marker and principal

axes increases the TRE value. This means that the TRE value in a particular area is affected by changing the location of fiducial markers. Additionally, we expect smaller TRE values with increased number of fiducial markers.

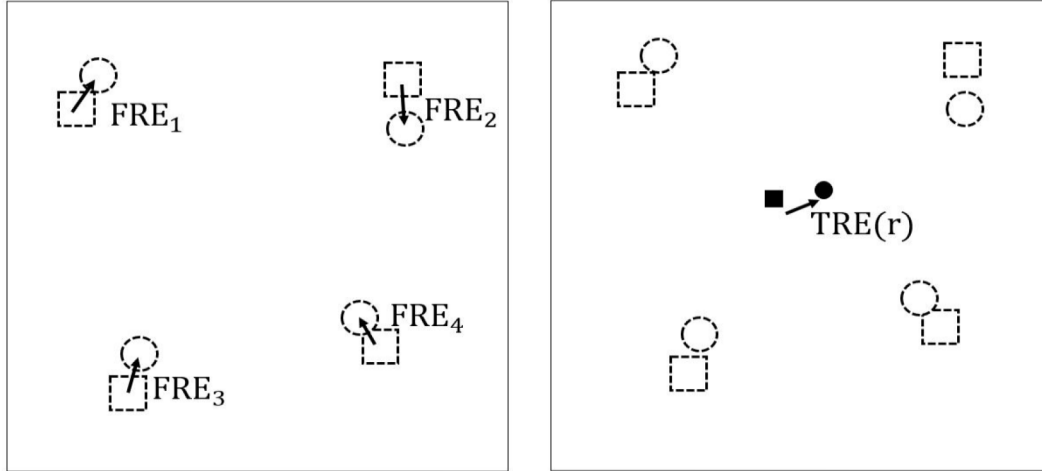


Figure 6. Schematic of point-based registration illustrating two measures of error. The FRE measured at each fiducial is the distance between the measured position of a fiducial in one space and its counterpart in the other space (dashed squares and dashed circles). The measured positions are points used in the registration. The TRE, measured at a point r relative to some given origin, is the distance after registration between the anatomical location (filled square) represented by r in one space and the corresponding anatomical point in the other space (filled circle).

3.2. Geometric calibration

The source and detector displacements in the CBCT C-arm system differ from a simple orbital path due to gravity-induced flex in the support arms. One way to overcome these unusual factors is to monitor the movement of the gantry in its rotation via either an external tracker or image-based calibration. The main goal of geometric calibration is to make the DRRs' generation capability from the mobile C-arm view. Therefore, this process calculates the homographic transformation between the tracker and the detector coordinate system ($T_{tracker}^{detector}$) is illustrated in Figure 7. The positions of the stainless steel spheres of the cylinder are precisely known from the calibration-phantom production process. The Xpoint stainless steel spheres and the CBCT images (3DRX volume) of the calibration-phantom are used to determine the relation between the reference marker and the calibration-phantom coordinate systems ($T_{marker}^{phantom}$):

$$T_{marker}^{phantom} = T_{CBCT}^{phantom} T_{marker}^{CBCT} \quad (3)$$

$T_{CBCT}^{phantom}$: Transformation from the 16 stainless steel spheres' geometry in the CBCT image to the corresponding 16 stainless steel spheres' positions in the calibration-phantom. This transformation depends on the localization of the spherical balls in the CBCT image.

T_{marker}^{CBCT} : Transformation from the 4 Xpoint stainless steel spheres' locations in the reference marker to the corresponding 4 stainless steel spheres positions' in the CBCT images. It was calculated by paired-point registration of these two sets of points.

Since the Xpoint reference marker is firmly attached to the calibration, this relationship is known and is assumed to be the identity matrix.

The relation between the coordinate systems of the video-optical tracker and the C-arm detector was calculated as:

$$T_{tracker}^{detector} = T_{phantom}^{detector} T_{marker}^{phantom} T_{tracker}^{marker} \quad (4)$$

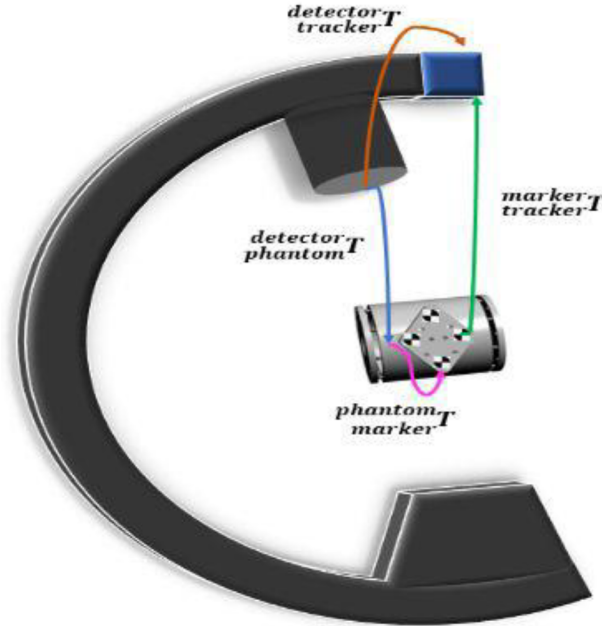


Figure 7. The relationship between transformations in the geometry calibration stage.

$T_{tracker}^{marker}$: Transformation from the video-optical tracker to the reference marker plate on the calibration-phantom was achieved by the video-optical tracker measurements.

$T_{phantom}^{detector}$: Transformation from the phantom calibration to the detector of the C-arm was calculated by Cho et al. [17]. One projection image of the calibration-phantom is adequate to provide the geometry or “pose” of the system. The procedure characterizes complete pose specifications at each projection angle. The value of this transformation is related to the mechanics of the gantry.

3.3. Calibration algorithm

The geometric calibration algorithm of Cho et al. [17] is used in this study as briefly described below. By placing the calibration-phantom in the imaging system, one CBCT image is taken and the projection image of two orbital patterns placed in a Plexiglas cylinder specifies two ellipses in the CBCT image, as shown in Figure 4b. All the geometric parameters of the system were calculated with respect to the parameters describing the two ellipses. The centers of the stainless steel spheres in the projection image were defined using the Canny operator by fitting two ellipses (with the standard form described in Eq. (5)) to the obtained data.

$$a(u - u_0)^2 + b(v - v_0)^2 + 2c(u - u_0)(v - v_0) = 1 \quad (5)$$

Here, (u_0, v_0) is the center of the ellipse and the parameters a, b, c, u_0, v_0 are calculated using a least squares algorithm. Therefore, the parameters of the system are calculated from parameters of the ellipses. Hence, the piercing point, detector angle, source position, detector position, and gantry angle are determined by the proposed algorithm of Cho et al. [17]. One X-ray is adequate to determine the pose of the system.

3.4. Artificial fluoroscopy

Artificial fluoroscopy reduces the amount of radiation exposed to the patient and surgical team by eliminating the demand for repetitious fluoroscopic imaging for placing the surgical tools.

Using DRRs generated from a CT image enables surgeons to see more easily and to interactively add or eliminate proposed seed positions from the treatment plan.

A DRR is the simulated 2D projection image from the volume data (e.g., CT or CBCT) using known views of the virtual camera.

The geometric accuracy of the DRRs is measured as projection error. The projection error is defined as the image distance between a projected point and a measured one.

The proposed combination uses the Siddon algorithm [21] for calculating DRR images. The purpose of the Siddon algorithm is to sum all the ray lengths through all voxels multiplied by voxel densities to obtain the radiological path.

$$\sum_{(i,j,k)} l(i,j,k) \cdot \rho(i,j,k) \quad (6)$$

The following two main applications of DRRs are specified:

1. The field of radiation therapy for the cure of cancer.
2. The field of computer-aided surgery (CAS).

The following chain of transformations is used to specify the DRR pose from the CT data. In this paper, we used DRRs created from a mobile C-arm perspective.

The DRRs created from a mobile C-arm perspective have been used to define the pose of artificial fluoroscopy based on the T_{CT}^{source} transformation. The relation between the coordinate system of the CT data and the X-ray source was calculated as:

$$T_{CT}^{source} = T_{detector}^{source} T_{tracker}^{detector} T_{marker}^{tracker} T_{CT}^{marker} \quad (7)$$

$T_{detector}^{source}$: Transformation from the coordinate system of the C-arm detector to the X-ray source (as acquired in the C-arm geometry calibration stage).

T_{CT}^{marker} : Transformation from the coordinate system of the CT data to the reference marker (as acquired in paired-point registration stage).

The relation between the coordinate system of the video-optical tracker and the C-arm detector ($T_{tracker}^{detector}$) was calculated using Eq. (4), and the relation of the video-optical tracker with the reference marker plate on the calibration-phantom ($T_{tracker}^{marker}$) was achieved by the video-optical tracker measurements.

4. Results

A CT scan of the spine phantom was acquired ($0.625 \times 0.625 \times 0.625 \text{ mm}^3$) and the fiducial markers in the lumbar vertebrae of the spine phantom were localized to subvoxel accuracy. The exact positions of the markers in the CT images, as well as on the phantom in physical space, were obtained using the Parsiss Image-Vision navigation system, and the other markers were considered as target markers. The registration markers were selected to be compatible with the number [22–24] and rules [19,25] of the combination of the markers. The fiducial markers and target locations were localized 20 times in the spine phantom and CT images using a

tracked pointer and the Parsiss Image-Vision navigation system to average 20 samples selected as fiducial and target locations [26–28]. TRE was measured to show the accuracy of the hybrid system in comparison with the conventional system. In the conventional system, the distance between the target and video-optical tracker was 100–200 cm, but this distance in the hybrid system was reduced to 60 cm (i.e. the video-optical tracker is fixed on the gantry of the mobile C-arm and the lens of the video-optical tracker is covered with lead glass for X-ray radiation protection).

4.1. Geometric accuracy of surgical tracking

The geometry accuracy in surgical instrument tracking with the proposed combination is summarized in Figures 8–10 and the Table. The box-and-whisker diagrams in Figures 8, 10, and 11 show the TRE median (red horizontal line inside the box), first and third quartiles (rectangular box), and total range (vertical lines with end caps).

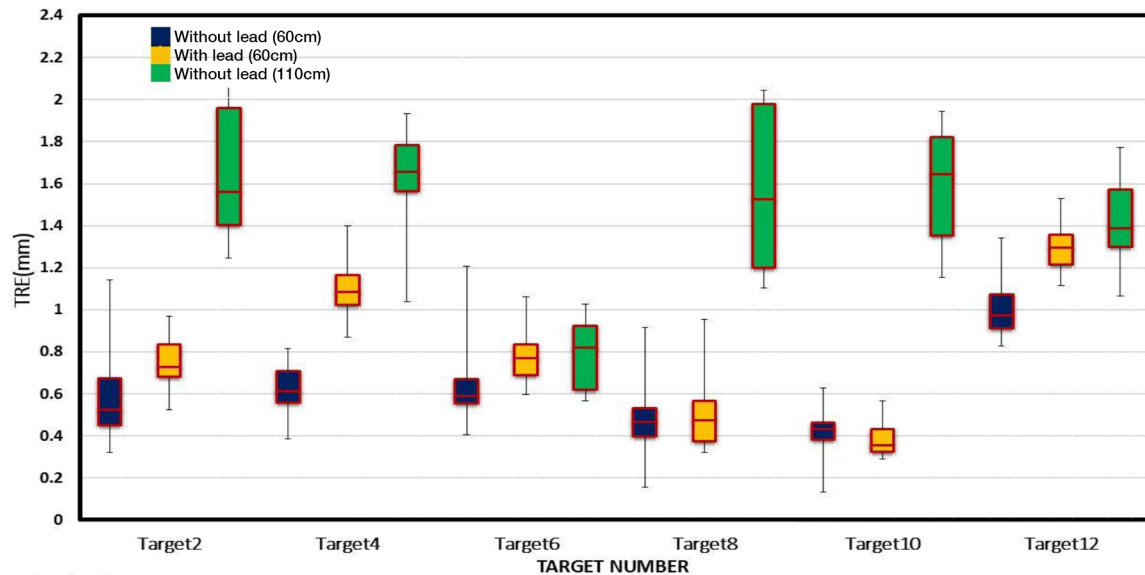


Figure 8. Measurement of target registration error with and without lead glass at a target-to-video optical tracker distance of ~ 60 cm demonstrated by the blue and yellow boxplots, respectively. Measurement of target registration error without lead glass at a target-to-video optical tracker distance of ~ 110 cm is shown by the green boxplot.

Table. Comparison of TRE measurements in various experiments.

Test	Description	Mean TRE (mm)
Lead glass	With lead glass	0.62 (± 0.20)
	Without lead glass	0.80 (± 0.34)
Video optical tracker-to-target distance	Conventional system	1.60 (± 0.43)
	Tracked C-arm system	0.80 (± 0.34)
Circular coordinate system	Pseudo C-arm Simulator	1.06 (± 0.09)
	Tracked C-arm system	1.17 (± 0.09)

The target registration error measurements with and without lead glass is illustrated in the boxplot of Figure 8. Paired t-tests show no statistically significant difference ($P = 0.11$) in the TRE measurements with

and without lead glass (0.62 ± 0.20 mm versus 0.80 ± 0.34 mm). Consequently, it provides the capability of tracking using the video-optical tracker covered with lead glass. Difference in the TRE measured with and without lead glass is due to the light reflection in the lead glass, which provides a certain systematic error.

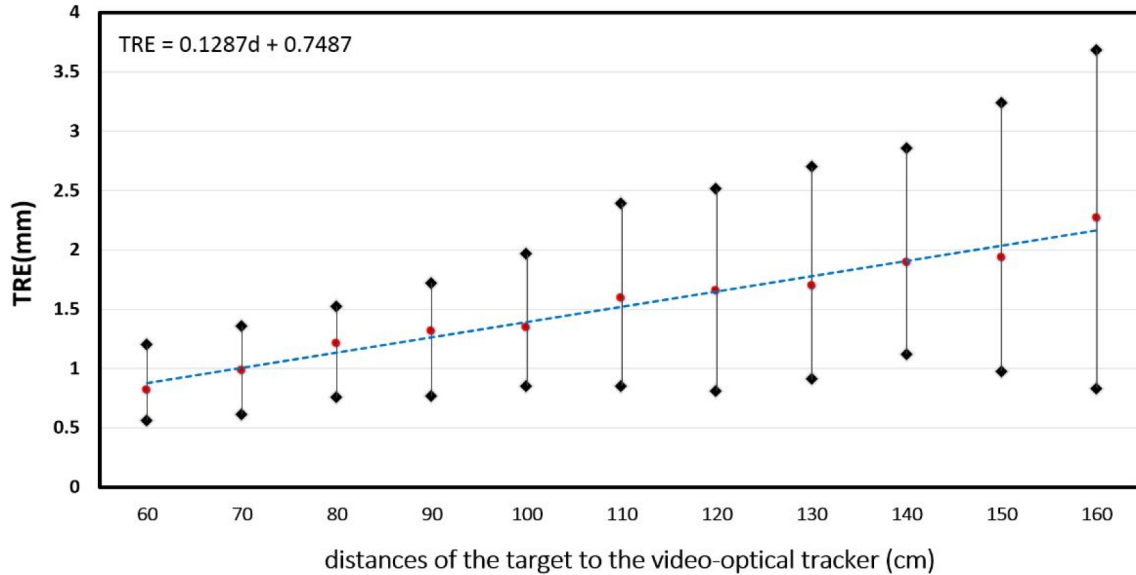


Figure 9. Measurement of target registration error as a function of video optical tracker-to-target distance. A linear fit to the measurements is superimposed.

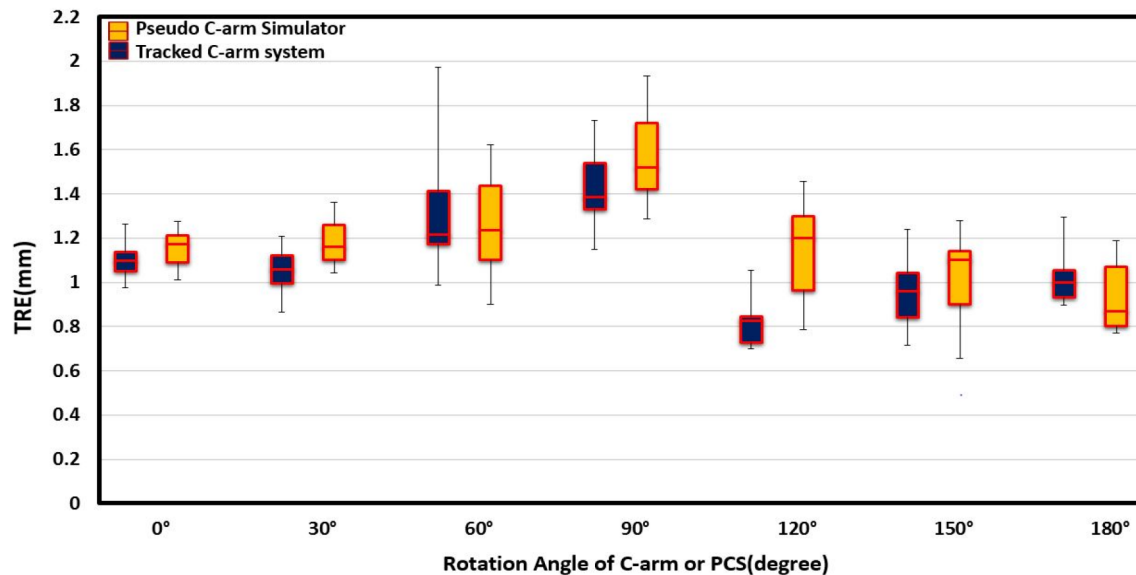


Figure 10. Comparison of TRE measurements in circular coordinate system of the PCS and the tracked C-arm setups demonstrated by the yellow and dark blue boxplots, respectively.

The TRE measurements at various video-optical tracker-to-target distances are illustrated in Figures 8 and 9. Figure 8 reports the TRE of the conventional system, in which the distance between the target and video-optical tracker was chosen as 110 cm, in comparison with the hybrid system with a distance value of 60

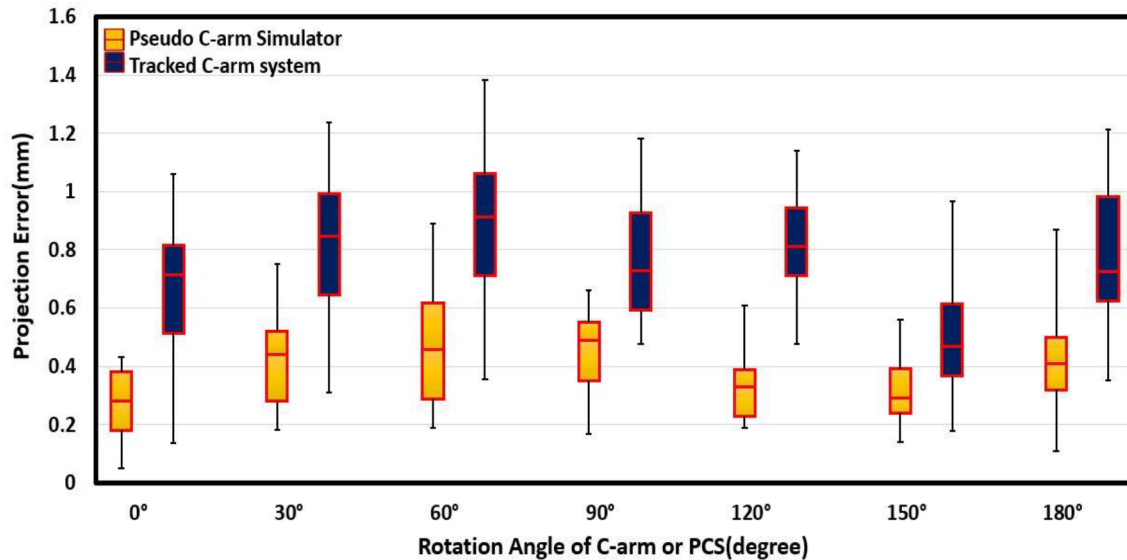


Figure 11. Comparison of projection error measurements of artificial fluoroscopy of the PCS and the tracked C-arm setups.

cm. The same video-optical tracker was used in both combinations. The proposed combination provides an improvement in the target registration error from 1.60 ± 0.43 mm to 0.80 ± 0.34 mm by almost 50%, which is statistically significant ($P < 0.0001$). The results obtained are consistent with the expected improvement in depth resolution at shorter video optical tracker-to-target distances.

Figure 9 shows the increase in the TRE as a linear function of tracker-to-target distance in the range of 60 to 160 cm with steps of 10 cm, increasing from 0.80 ± 0.34 mm at 60 cm to 2.26 ± 0.21 mm at 160 cm. The experiment was performed in the laboratory setup on the experimental table with a stand-alone tracker. The results obtained from this study are consistent with other works that have proved that the depth measurement error depends on the distance to the target [29–31]. Due to the limited field of view of the video-optical tracker, the TRE could not be calculated at distance of less than 60 cm.

The geometric accuracy of the hybrid system is achieved over rotation of the PCS and the tracked C-arm setups (with steps of 30°). Hence, the “six-facet” reference marker is attached to the spine phantom to simulate the PCS and the tracked C-arm setup rotations. Figure 10 shows the TRE measurement in the frame of reference (using the “six-facet” reference marker), including measurements performed on the PCS (yellow) and the tracked C-arm setups (blue). The stability of TRE measurements for the PCS and the tracked C-arm setups over 180° rotation demonstrates the capability of the “six-facet” reference marker to retain registration within the circular framework. There was no statistically significant difference in TRE measurements ($P = 0.17$) between the PCS and the tracked C-arm setups: 1.06 ± 0.09 mm versus 1.17 ± 0.09 mm, respectively.

4.2. Geometric accuracy of digitally reconstructed radiograph

The PCS and tracked C-arm setups provide the ability to create the DRR (i.e. artificial fluoroscopy). Geometric accuracy of artificial fluoroscopy is measured in terms of projection error (i.e. the difference between the location of the stainless steel sphere in real and artificial fluoroscopy). The Siddons method enables real-time DRR generation from the 3D data set of either the preoperative CT or intraoperative CBCT [21]. The 3D images of CT and CBCT of the calibration-phantom were acquired. The stainless steel spheres in the real and the

artificial fluoroscopy are segmented by Hough transform edge detection to obtain the projection error between the real and virtual location of stainless steel spheres. Therefore, for geometric accuracy, quantitative evaluation is provided. Because of the “six-facet” reference marker, the geometric accuracy is independent of the rotation angle of PCS or tracked C-arm setups. The yellow boxplot in Figure 11 shows the projection error over 180° rotation of the PCS setup (with steps of 30°) and suggests a reasonable correspondence between the real and virtual projections, with a projection error of 0.4 ± 0.32 mm. The blue boxplot in Figure 11 quantifies the geometric accuracy of artificial fluoroscopy in the tracked C-arm system. The projection error measured in the 16 stainless steel spheres on the calibration-phantom was 0.74 ± 0.13 mm across all C-arm angles. The DRRs reconstructed from the CBCT data result in a lower image quality compared to the DRRs reconstructed from the CT data. Due to the reduced number of projections for image reconstruction, the CBCT data caused limited image quality compared to the CT data.

5. Discussion and conclusions

The proposed hybrid system has provided a variety of capabilities, including surgical tracking and generation of DRRs from the mobile C-arm perspective, rather than conventional systems in the operating room. There was no statistically significant difference in the TRE measured due to covering the video-optical tracker with lead glass to protect the tracker lens from X-ray radiation damage. To retain registration within a circular framework, a “six-facet” reference marker visible over all rotation angles of the C-arm system or PCS setup is proposed, and the hybrid system is shown to provide improved TRE values in comparison with conventional systems. The proposed system reduces line-of-sight curtailment due to personnel presence around the surgical operating table. The tracked C-arm system capability using DRRs (e.g., the artificial fluoroscopy generated from any C-arm angulation) demonstrated submillimeter accuracy. The “six-facet” reference marker thereby retains tracking and artificial fluoroscopy capabilities as the C-arm rotates about the surgical operating table for CBCT or fluoroscopy. The tracked C-arm system was used effectively in a wide variety of surgeries, such as spine surgeries in which the surgeons insert a screw or needle, vertebroplasty, and kyphoplasty. In terms of reduced radiation exposure, it was demonstrated that the C-arm positioning in the conventional system requires 2–7 radiographic images in comparison with our tracked C-arm system, which required 0–2 images. Although the tracked C-arm system reduced line-of-sight curtailment, it presented implications for marker designs to provide tracking at mobile C-arm arbitrary angles.

Using DRR capacities generated from 3D images (CT and CBCT) provided target anatomy localization without X-ray radiation. In addition, this capability enabled visualization of the projection views without radiation exposure at arbitrary angles of the mobile C-arm. Artificial fluoroscopy provided here has shown advantages over conventional fluoroscopy while providing suitable targeting precision. This system allows the mobile C-arm to potentially provide real-time multiple-plane guidance. It also minimizes the amount of radiation exposure to the patient and surgical staff by omitting the need for repetitive repositioning of the fluoroscope to get multiplanar guidance.

The proposed integration of the tracked C-arm system potentially is useful for image-guided surgery systems that need simultaneous use of CBCT and surgical tracking. Overall, ongoing work has provided improvements in visualization and geometric accuracy and also reduced line-of-sight curtailment and radiation exposure.

Future work includes implementation in the Parsiss Image-Vision navigation system and evaluates the accuracy, radiation exposure, and X-ray exposure time in surgical procedures.

Acknowledgment

We would like to gratefully acknowledge the Research Centre of Biomedical Technology and Robotics, of Tehran University of Medical Sciences, and the Image Guided Intervention Group of this Research Centre for providing invaluable resources.

References

- [1] Boszczyk BM, Bierschneider M, Panzer S, Panzer W, Harstall R, Schmid K, Jaksche H. Fluoroscopic radiation exposure of the kyphoplasty patient. *Eur Spine J* 2006; 15: 347-355.
- [2] Rampersaud YR, Foley KT, Shen AC, Williams S, Solomito M. Radiation exposure to the spine surgeon during fluoroscopically assisted pedicle screw insertion. *Spine* 2000; 25: 2637-2645.
- [3] Synowitz M, Kiwit J. Surgeon's radiation exposure during percutaneous vertebroplasty. *J Neurosurg-Spine* 2006; 4: 106-109.
- [4] Theocharopoulos N, Perisinakis K, Damilakis J, Papadokostakis G, Hadjipavlou A, Gourtsoyiannis N. Occupational exposure from common fluoroscopic projections used in orthopaedic surgery. *J Bone Joint Surg* 2003; 85: 1698-1703.
- [5] Foley KT, Simon DA, Rampersaud YR. Virtual fluoroscopy: computer-assisted fluoroscopic navigation. *Spine* 2001; 26: 347-351.
- [6] Euler E, Heining S, Riquarts C, Mutschler W. C-arm-based three-dimensional navigation: a preliminary feasibility study. *Comput Aided Surg* 2003; 8: 35-41.
- [7] van de Kraats EB, Carelsen B, Fokkens WJ, Boon SN, Noordhoek N, Niessen WJ, van Walsum T. Direct navigation on 3D rotational x-ray data acquired with a mobile propeller C-arm: accuracy and application in functional endoscopic sinus surgery. *Phys Med Biol* 2005; 50: 5769.
- [8] van de Kraats EB, Walsum Tv, Kendrick L, Noordhoek NJ, Niessen WJ. Accuracy evaluation of direct navigation with an isocentric 3D rotational X-ray system. *Med Image Anal* 2006; 10: 113-124.
- [9] Sorensen S, Mitschke M, Solberg T. Cone-beam CT using a mobile C-arm: a registration solution for IGRT with an optical tracking system. *Phys Med Biol* 2007; 52: 3389.
- [10] Feuerstein M, Mussack T, Heining SM, Navab N. Intraoperative laparoscope augmentation for port placement and resection planning in minimally invasive liver resection. *IEEE T Med Imaging* 2008; 27: 355-369.
- [11] Kotani Y, Abumi K, Ito M, Takahata M, Sudo H, Ohshima S, Minami A. Accuracy analysis of pedicle screw placement in posterior scoliosis surgery: comparison between conventional fluoroscopic and computer-assisted technique. *Spine* 2007; 32: 1543-1550.
- [12] Laine T, Lund T, Ylikoski M, Lohikoski J, Schlenzka D. Accuracy of pedicle screw insertion with and without computer assistance: a randomised controlled clinical study in 100 consecutive patients. *Eur Spine J* 2000; 9: 235-240.
- [13] Rajasekaran S, Vidyadhara S, Ramesh P, Shetty AP. Randomized clinical study to compare the accuracy of navigated and non-navigated thoracic pedicle screws in deformity correction surgeries. *Spine* 2007; 32: E56-E64.
- [14] Ritter D, Mitschke M, Graumann R. Markerless navigation with the intra-operative imaging modality SIREMOBIL Iso-C3D. *Electromedica* 2002; 70: 31-36.
- [15] Dressel P, Wang L, Kutter O, Traub J, Heining SM, Navab N. Intraoperative positioning of mobile C-arms using artificial fluoroscopy. In: *IEEE 2010 SPIE Medical Imaging*; 23 February 2010; San Diego, CA, USA. Bellingham, WA, USA: IEEE. pp. 762506-762506.
- [16] Navab N, Heining SM, Traub J. Camera augmented mobile C-arm (CAMC): Calibration, accuracy study, and clinical applications. *IEEE T Med Imaging* 2010; 29: 1412-1423.
- [17] Cho Y, Moseley DJ, Siewerdsen JH, Jaffray DA. Accurate technique for complete geometric calibration of cone-beam computed tomography systems. *Med Phys* 2005; 32: 968-983.

- [18] Arun KS, Huang TS, Blostein SD. Least-squares fitting of two 3-D point sets. *IEEE T Pattern Anal* 1987; 9: 698-700.
- [19] West JB, Fitzpatrick JM, Toms SA, Maurer Jr CR, Maciunas RJ. Fiducial point placement and the accuracy of point-based, rigid body registration. *Neurosurgery* 2001; 48: 810-817.
- [20] Fitzpatrick JM, West JB. The distribution of target registration error in rigid-body point-based registration. *IEEE T Med Imaging* 2001; 20: 917-927.
- [21] Siddon RL. Fast calculation of the exact radiological path for a three-dimensional CT array. *Med Phys* 1985; 12: 252-255.
- [22] Labadie RF, Shah RJ, Harris SS, Cetinkaya E, Haynes DS, Fenlon MR, Juszczak AS, Galloway RL, Fitzpatrick JM. In vitro assessment of image-guided otologic surgery: submillimeter accuracy within the region of the temporal bone. *Otolaryng Head Neck* 2005; 132: 435-442.
- [23] Strong EB, Rafii A, Holweg-Majert B, Fuller SC, Metzger MC. Comparison of 3 optical navigation systems for computer-aided maxillofacial surgery. *Otolaryng Head Neck* 2008; 134: 1080-1084.
- [24] Fried MP, Kleefield J, Gopal H, Reardon E, Ho BT, Kuhn FA. Image-guided endoscopic surgery: results of accuracy and performance in a multicenter clinical study using an electromagnetic tracking system. *Laryngoscope* 1997; 107: 594-601.
- [25] Hamming NM, Daly MJ, Irish JC, Siewerdsen JH. Effect of fiducial configuration on target registration error in intraoperative cone-beam CT guidance of head and neck surgery. In: *IEEE 2008 Engineering in Medicine and Biology Society*; 20–25 August 2008; Vancouver, Canada. Piscataway, NJ, USA: IEEE. pp. 3643-3648.
- [26] Maier-Hein L, Tekbas A, Seitel A, Pianka F, Müller SA, Satz S, Schawo S, Radeleff B, Tetzlaff R, Franz AM. In vivo accuracy assessment of a needle-based navigation system for CT-guided radiofrequency ablation of the liver. *Med Phys* 2008; 35: 5385-5396.
- [27] Birkfellner W, Solar P, Gahleitner A, Huber K, Kainberger F, Kettenbach J, Homolka P, Diemling M, Watzek G, Bergmann H. In-vitro assessment of a registration protocol for image guided implant dentistry. *Clin Oral Implan Res* 2001; 12: 69-78.
- [28] Labadie RF, Shah RJ, Harris SS, Cetinkaya E, Haynes DS, Fenlon MR, Juszczak AS, Galloway RL, Fitzpatrick JM. Submillimetric target-registration error using a novel, non-invasive fiducial system for image-guided otologic surgery. *Comput Aided Surg* 2004; 9: 145-153.
- [29] Blostein SD, Huang TS. Error analysis in stereo determination of 3-D point positions. *IEEE T Pattern Anal* 1987; 9: 752-765.
- [30] Chang C, Chatterjee S. Quantization error analysis in stereo vision. In: *IEEE 1992 Signals, Systems and Computers*; 26–28 October 1992; Pacific Grove, CA, USA. New York, NY, USA: IEEE. pp. 1037-1041.
- [31] Gallup D, Frahm JM, Mordohai P, Pollefeys M. Variable baseline/resolution stereo. In: *IEEE 2008 Computer Vision and Pattern Recognition*; 23–28 June 2008; Anchorage, AK, USA. Fort Collins, CO, USA: IEEE. pp. 1-8.